Journal of Applied Fluid Mechanics, Vol. 19, No. 1, pp. 3354-3367, 2026. Available online at <a href="https://www.jafmonline.net">www.jafmonline.net</a>, ISSN 1735-3572, EISSN 1735-3645. <a href="https://doi.org/10.47176/jafm.19.1.3618">https://doi.org/10.47176/jafm.19.1.3618</a>



# Effect of Boundary-layer Suction on the Performance of an Intake under Off-design Condition

Y. Zhang<sup>1</sup>, D. Yang<sup>1</sup>, B. Dong<sup>1†</sup> and S. Wang<sup>2</sup>

<sup>1</sup> High Speed Aerodynamics Institute, China Aerodynamics Research and Development Center, Mianyang 621000, China <sup>2</sup> School of Mechanical, Electronic and Control Engineering, Beijing Jiaotong University, Beijing 100044, China

†Corresponding Author Email: dongbin@cardc.cn

#### **ABSTRACT**

Under off-design conditions, shock wave-boundary layer interaction (SWBLI) and large-scale separation within the intake become prominent, leading to significant decrease in aerodynamic performance. By introducing a boundary layer suction system, numerical calculations are used to investigate the variations in flow and performance, and to analyze the suction mechanism. Boundary layer suction effectively removes low kinetic energy fluid, reduces the size of the separation bubble size, relieves the pressure gradient, and transforms the bow shock at the inlet into an incident oblique shock. At the same time, the suction device can also increase the total pressure recovery ratio (TPR), and the captured mass flow ratio (CMFR), while reducing the distortion index (DI). In particular, different suction locations and numbers, as well as backpressures, affect the flow field differently. The S2 is key in controlling the cowl-incident shock wave and separating bubble. Its suction action can change the type of shock interaction at the inlet from  $\lambda$ -type to x-type. Therefore, the reasonable setting of suction holes can enhance the aerodynamic performance and operating stability of the intake by optimizing the internal shock wave system.

# Article History

Received April 23, 2025 Revised August 16, 2025 Accepted August 19, 2025 Available online November 5, 2025

# Keywords:

Shock wave-boundary layer interaction Supersonic intake Off-design condition Large-scale separation Boundary layer suction Aerodynamic performance Pressure gradient

# 1. Introduction

The supersonic intake is a crucial component of a ramjet engine, and its performance directly affects the operational efficiency and stability of the entire vehicle. Under high maneuverability and multi-mission adaptability background, intakes often undergo severe tests in off-design conditions during actual flight. Under off-design conditions, the flow inside the intake is complex and variable. Phenomena such as shock waveboundary layer interaction (SWBLI) and large-scale separation are frequently occurring, and many vortices in the separation zone cause total pressure loss and nonuniformity in the flow field (Fisher, 1986; Zhou et al., 2019; Wang et al., 2015). In some cases, it even blocks the inlet and generates a bow shock wave, resulting in nonstart and a significant drop in aerodynamic performance. It has become a significant constraint on the vehicle's performance.

In the aerodynamic phenomenon of the intake, blockage due to several factors often allows the production of a non-start. When it occurs, a normal or bow shock is usually induced in front of the cowl. The overflow results in a significant reduction in the captured mass flow ratio

(CMFR) and total pressure recovery (TPR). Among them, the non-start caused by the geometrical effect is primarily characterized by the boundary layer separation caused by SWBLI, which creates a blockage effect at the inlet. The other type of non-start is induced by the upward shift of the shock train to the inlet formed by the high backpressure generated in the combustion chamber (Hirschen et al., 2007). However, it is worth noting that SWBLI is the primary triggering mechanism for non-start in the presence of an incident shock wave at the cowl. Therefore, additional devices are essential to control the intensity of SWBLI and to improve the intake performance.

Many investigations on intake flow control and improvement have been conducted in the existing literature, including upstream flow conditions (Herrmann et al., 2011), the no-start phenomenon (Chen et al., 2019), and buzzing oscillations (Abedi et al., 2020a; Yamamoto et al., 2020). The standard features of these aerodynamic problems are SWBLI and the induced separation bubble. Currently, the most popular control methods for shoulder flow separation include shoulder bumps (Tian et al., 2023; Schülein et al., 2022; Zhang et al., 2019), vortex generators (Zhang et al., 2015; Khan et al., 2023;

| NOMENCLATURE    |   |                      |  |  |  |  |
|-----------------|---|----------------------|--|--|--|--|
| a, b, e, f      | starting points of the compression corner, cowl, isolation, and diffusion | $p_{\theta}$         | total pressure   |  |  |  |
| BMFR            | bleed mass flow ratio   | $p_{\infty}$         | static pressure of freestream                              |  |  |  |
| $B_1, B_2, B_3$ | action points of barrier shock wave by $S_1$ , $S_2$ , $S_3$              | $p_{suc}$            | backpressure of suction chamber                            |  |  |  |
| CMFR            | captured mass flow ratio  | Re                   | unit Reynolds number                                       |  |  |  |
| D               | diameter of suction hole  | $Q_{sonic}$          | sonic flow coefficient                                     |  |  |  |
| DI              | distortion index  | $S_1, S_2, S_3, S_4$ | suction holes at different locations                       |  |  |  |
| h               | height of throat  | T                    | static temperature   |  |  |  |
| $I_1, I_2$      | action points of background wave system                                   | $T_{0}$              | total temperature  |  |  |  |
| Ма              | Mach number   | TPR                  | total pressure recovery                                    |  |  |  |
| p               | static pressure   | x, y                 | Cartesian coordinates (streamwise and vertical directions) |  |  |  |
| Subscripts      | S   |                      | •  |  |  |  |
| in              | entrance "b".   | 0                    | total condition  |  |  |  |
| iso             | isolation "c"   | $\infty$             | static condition   |  |  |  |
| suc             | suction chamber condition   | theory               | theoretical condition                                      |  |  |  |

Narayanaswamy & Funderburk, 2019), and boundary layer suction and bleeding (Soltani et al., 2015; Soltani et al., 2016; Wang et al., 2021). Boundary layer suction has recently garnered significant attention as an effective flow control technique. By positioning the suction device in a specific area of the inlet and removing part of the low kinetic energy fluid from the boundary layer, the local flow structure can be altered and the separation scale can be reduced, thereby optimizing the aerodynamic performance of the intake. This technology offers significant control effectiveness and easy adjustment, providing a broad application prospect. Numerous experimental and numerical studies have investigated suction devices, demonstrating that suction slots effectively eliminate large-scale separation zones under adverse pressure gradients (He et al., 2017; Sethuraman et al., 2021). Liou & Benson (2010) conducted an early numerical study on the design optimization of bleeding, considering the improvement of TPR. However, the target geometries were double-wedge ramps and flat plates rather than the entire supersonic intake. Herrmann et al. (2013) experimentally investigated the performance of a rectangular ramjet intake with a boundary layer suction system to examine the pressure oscillations at the critical state. Giehler et al. (2024) evaluated the suction efficiency and boundary layer removal effect within a simplified turbulent boundary layer. The effects of porosity, staggering angle, and hole diameter were investigated, and it was demonstrated that the hole depth-to-diameter ratio is the key factor in determining suction efficiency. Choe et al. (2020) calculated the effect of suction in a supersonic intake. Numerical results and genetic algorithms were employed to obtain the best suction conditions, enhance the TPR, and optimize performance.

In addition to the suction device's dimensions, the location of the suction holes is also important for overall intake performance. Studies have been conducted on various locations, including the compression surface/center body, cowl, sidewall, and diffuser (Fisher, 1986; Titchener & Babinsky, 2013; Zuo & Huang, 2018; Zhang et al., 2020). Soltani et al. (2015) proposed that the

effectiveness of the suction system is higher when the holes are applied near the SWBLI and close to the throat. On the other hand, Chen et al. (2019) used several narrow suction slots on the compression surface to suppress intake buzz. These studies have shown that the compression surface and the shoulder region are crucial for controlling the intake suction. Significant advantages exist for suction in the shoulder region. The pressure rise induced by the cowl-incident shock will drive the low-energy airflow into the suction chamber. At the same time, it can suppress the possible separation zone due to SWBLI in the throat, thus improving the starting characteristics. Therefore, Pattnaik and Rajan (2022) numerically investigated the effect of some geometrical parameters of the suction slots in the shoulder region (including the area of the slots, the vertical height, and the position of the incident shock) on the performance of a supersonic intake. The results showed that the flow field uniformity and the TPR at the outlet were significantly improved for all operating conditions through the suction device. Considering the effect of the position relative to the incident shock wave on the amount of suction required to eliminate the separation, Fukuda et al. (1977) and Wong (1974) concluded that the suction position upstream or downstream of the pressure rise induced by the shock wave is more helpful in eliminating the separation and obtaining better performance than that at the shock wave position. Whereas Hamed et al. (1995) conducted a detailed numerical study, showing that the position of the incident point is optimal for controlling the separation and minimizing the resulting mass loss. In a recent study, Zhang et al. (2025) proposed that suction at the incident point achieves the best control of the separation zone and minimizes the adverse pressure gradient through an expansion corner.

The above studies have shown that boundary layer suction can improve the intake's complex flow and non-starting characteristics under the off-design condition. Flow separation, commonly occurring under the continuous action of expansion and compression waves, typically takes place at the inlet, making local suction a significant factor in the effects of SWBLI and large-scale

separation. Aiming to investigate the suction effect in the shoulder region of a typical rectangular intake under off-design conditions, the variation of the separation region and characteristics under different suction positions is investigated by numerical methods. Section 2 describes the numerical method and intake models with numerical validation. Section 3 presents and discusses the flow field structure and changes in aerodynamic performance under suction. Finally, the main conclusions of the study are given in Section 4.

#### 2. COMPUTATIONAL DETAIL

#### 2.1 Intake Model and Suction System Design

This study employed a rectangular intake with two compression stages, and the main dimensional parameters are illustrated in Fig. 1. The compression surfaces of the two stages are 16° and 14°, respectively. The total length of the compression surfaces is 208 mm, and the length of the primary compression surface is 167 mm. The compression shock wave converging on the cowl was designed for Ma=4. The Ma is defined as the ratio of flow velocity to local sound velocity. The shoulder of the intake is transitioned by rounded arcs with a radius of 77 mm and 104 mm. The isolation section has a length of 61 mm and a height of h=19 mm. In all subsequent studies, the dimensions have been normalized with h. At the intersection of the isolation and diffusion, an expansion step with an angle of 10° and length of 1.5 mm exists on the lower surface. It is not shown in the main view of Fig. 1 for resolution reasons. Two diffuser sections increase the height of the channel from 19 mm to 45 mm and 105 mm, and the total length of the diffuser section is 473 mm. The total length of the model is 790 mm.

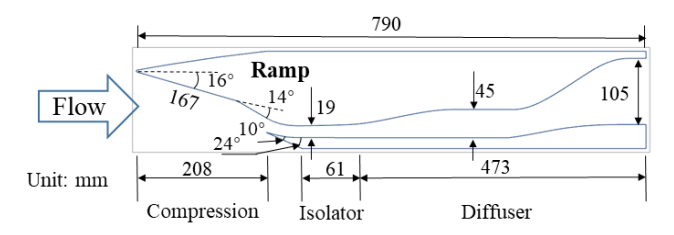


Fig. 1 Schematic diagram of the 2D intake model

Typical rectangular intake often uses a 2D crossfor numerical calculations to improve computational efficiency (Kwak and Lee, 2013). Abedi et al. (2020b) showed in their steady-state numerical analysis that 3-D effects don't significantly impact intake performance. The sidewall effects are not considered, and the rectangular intake in Fig 1 has a strong twodimensional effect, so its centerline cross-section is extracted for numerical calculation. The overall computational domain is shown in Fig. 2. To provide accurate boundary conditions, external flow regions were created above, below, and in the spanwise direction of the intake, ranging from approximately 10, 8, and 15 times the height h of the isolation. The boundary of the external area is so placed to ensure that the compression shock can pass through the external boundary and avoid reflection of any shock. Pressure far-field and pressure outlet conditions are

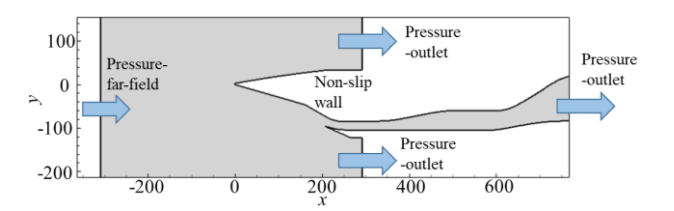


Fig. 2 Computational domain and boundary conditions

Table 1 Incoming flow conditions

| Ма | $T_0(\mathbf{K})$ | T(K) | $p_0$ (kpa) | $p_{\infty}$ (kpa) |
|----|-------------------|------|-------------|--------------------|
| 3  | 288               | 103  | 360         | 9.8                |

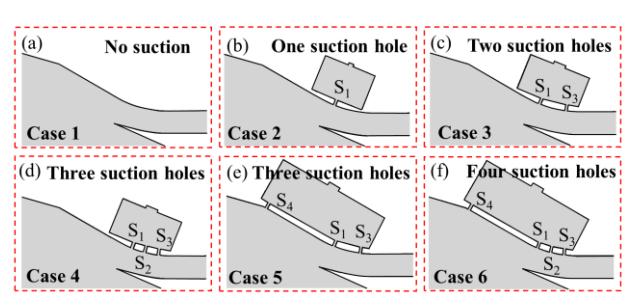


Fig. 3 Schematic of the (a) base model and (b-f) different boundary layer suction

used for the inlet and outlet of the computational domain, respectively. No-slip wall conditions are used for both intake walls. The incoming flow conditions are shown in Table 1. The SWBLI and large-scale separation under off-design conditions are investigated, with the selected Mach number of the incoming flow being Ma=3, the total pressure being  $p_0=360$  kpa, and the total temperature being  $T_0=288$  K. The resulting unit Reynolds number is  $Re=2.85\times10^7$  m<sup>-1</sup>.

In the off-design condition, the shoulder region is often associated with a large-scale separation bubble induced by the incident shock at the cowl, which results in a significant reduction of the aerodynamic throat height. This phenomenon will result in a decrease in aerodynamic performance, which will be further discussed in Section 3. To improve the phenomenon, suction holes are positioned in the shoulder region or in the compression corner region to remove low-kinetic-energy fluids from the boundary layer, thereby enhancing the localized flow conditions. The specific boundary layer suction scheme is shown in Fig. 3. Case 1 is the base model without the suction device. Five schemes (Case 2-Case 6) with one to four holes were used for the suction device. All holes have a diameter of D=2mm. Based on the locations, the four suction holes were named S<sub>1</sub>-S<sub>4</sub>. The S<sub>1</sub>-S<sub>3</sub> are located at 23%, 47%, and 70% of the arc segment. The S<sub>4</sub> was located 2 mm downstream of the compression corners to remove the backflow zone. Corresponding chambers are attached above each of the suction holes. An outlet is located above the chamber to apply suction backpressure  $p_{\text{suc}}$ .

#### 2.2 Numerical Methods

The calculations were performed using ANSYS Fluent 19.0 in a density-based, double-precision, 2D

compressible formulation. The Reynolds-averaged Navier-Stokes (RANS) equations were solved via the finite volume method (FVM) (Alfonsi, 2009), employing a coupled implicit solver for steady-state flow. The governing equations are as follows:

$$\frac{\partial \rho}{\partial t} + \frac{\partial (\rho u)}{\partial x} + \frac{\partial (\rho v)}{\partial y} = 0 \tag{1}$$

$$\begin{bmatrix}
\frac{\partial(\rho u)}{\partial t} + \frac{\partial(\rho u^{2} + p)}{\partial x} + \frac{\partial(\rho uv)}{\partial y} = \frac{\partial}{\partial x} \left[ (\mu + \mu_{t}) \left( 2 \frac{\partial u}{\partial x} - \frac{2}{3} \nabla U \right) \right] \\
+ \frac{\partial}{\partial y} \left[ (\mu + \mu_{t}) \left( \frac{\partial u}{\partial y} + \frac{\partial v}{\partial x} \right) \right] \\
\frac{\partial(\rho v)}{\partial t} + \frac{\partial(\rho v^{2} + p)}{\partial y} + \frac{\partial(\rho uv)}{\partial x} = \frac{\partial}{\partial y} \left[ (\mu + \mu_{t}) \left( 2 \frac{\partial v}{\partial y} - \frac{2}{3} \nabla U \right) \right] \\
+ \frac{\partial}{\partial x} \left[ (\mu + \mu_{t}) \left( \frac{\partial v}{\partial x} + \frac{\partial u}{\partial y} \right) \right]$$
(2)

$$\frac{\partial(\rho E)}{\partial t} + \frac{\partial\left[u(\rho E + p)\right]}{\partial x} + \frac{\partial\left[v(\rho E + p)\right]}{\partial y} = \frac{\partial}{\partial x}\left[\left(\kappa + \kappa_{t}\right)\frac{\partial T}{\partial x}\right] \\
+ \frac{\partial}{\partial y}\left[\left(\kappa + \kappa_{t}\right)\frac{\partial T}{\partial y}\right] + \frac{\partial}{\partial x}\left(u\tau_{xx} + v\tau_{yx}\right) + \frac{\partial}{\partial y}\left(u\tau_{xy} + v\tau_{yy}\right)$$
(3)

where U is the velocity vector,  $\kappa$  is the molecular thermal conductivity,  $\kappa_t$  is the turbulent thermal conductivity,  $\tau$  is the Reynolds stress. The Reynolds stress component can be expressed as:

$$\begin{cases} \tau_{xx} = (\mu + \mu_t) \left( 2 \frac{\partial u}{\partial x} - \frac{2}{3} \nabla \Box U \right) \\ \tau_{xy} = \tau_{yx} = (\mu + \mu_t) \left( \frac{\partial u}{\partial y} + \frac{\partial v}{\partial x} \right) \\ \tau_{yy} = (\mu + \mu_t) \left( 2 \frac{\partial v}{\partial y} - \frac{2}{3} \nabla \Box U \right) \end{cases}$$
(4)

In the RANS method, turbulent stress and heat fluxes are modelled using a minimum number of equations, thus reducing the calculation effort. The RANS equations are solved by the k- $\omega$  SST turbulence model, which can combine the advantages of k- $\omega$  in the near-wall region and k- $\varepsilon$  in the core flow region outside the boundary layer, as described by Wilcox (1998). The model can accurately predict flow separation under adverse pressure gradients. The transport equations for turbulent kinetic energy and specific dissipation rate are as follows:

$$\frac{\partial(\rho k)}{\partial t} + \frac{\partial(\rho u k)}{\partial x} + \frac{\partial(\rho u k)}{\partial y} = P_k - \beta^* \rho \omega k + \frac{\partial}{\partial x} \left[ (\mu + \sigma_k \mu_t) \frac{\partial k}{\partial x} \right] + \frac{\partial}{\partial y} \left[ (\mu + \sigma_k \mu_t) \frac{\partial k}{\partial y} \right]$$
(5)

$$\frac{\partial(\rho\omega)}{\partial t} + \frac{\partial(\rho\omega\omega)}{\partial x} + \frac{\partial(\rho\omega\omega)}{\partial y} = \frac{\gamma_t}{\nu_t} P_k - \beta\rho\omega^2 + \frac{\partial}{\partial x} \left[ (\mu + \sigma_\omega \mu_t) \frac{\partial\omega}{\partial x} \right] \\
+ \frac{\partial}{\partial y} \left[ (\mu + \sigma_\omega \mu_t) \frac{\partial\omega}{\partial y} \right] + 2(1 - F_1) \rho\sigma_{\omega 2} \frac{1}{\omega} \left( \frac{\partial k}{\partial x} \frac{\partial\omega}{\partial x} + \frac{\partial k}{\partial y} \frac{\partial\omega}{\partial y} \right) \tag{6}$$

where  $\sigma_k$ ,  $\sigma_\omega$ ,  $\beta$  and  $\gamma$  are model constants, the exact values of which can be found from Menter (1994). The  $F_1$  is the mixing function.

The time integral method used an implicit dual-time stepping method, the inviscid terms are discretized using

a second-order upwind Roe flux difference splitting scheme, and the viscous terms are treated with a second-order central difference format.

Under the calculation condition, the incoming flow is modelled as an ideal gas since the stagnation temperature is kept below 700 K. The properties of the gas are defined as a function of temperature, such as specific heat capacity  $C_p$ , thermal conductivity  $\lambda$  and viscosity  $\mu$ . Where  $\mu$  is defined by using Sutherland's formula. The model and the corresponding parameters are given below:

$$\mu = \mu_c \frac{T_0 + C}{T + C} (\frac{T}{T_0})^{1.5} \tag{7}$$

$$C_n = 955.63 + 0.176T \tag{8}$$

$$\lambda = \mu C_{\nu} (1.32 + \frac{1.77R}{C_{\nu}}) \tag{9}$$

where  $T_c$  is the reference temperature, which is 288 K;  $\mu_c$  is the reference viscosity at the reference temperature, which is  $1.72 \times 10^{-5}$  Pa·s; C is the Sutherland's constant, which is 110 K; R is the gas constant, which is 287 (J/(kg·K));  $C_p$  and  $C_v$  are the specific heats at constant pressure and constant specific heat capacity, respectively.

# 2.3 Numerical Validation and Mesh Independence

To further ensure the effect of uncertainties in the turbulence model and boundary conditions, Herrmann and Koschel (2002) validated the numerical method with experimental data of a supersonic intake. The model consists of a compression surface, cowl, throat, and diffuser. More detailed information on the geometry can be found in Herrmann and Koschel (2002). Numerical calculations were conducted under the experimental condition of Ma=2.5,  $p_0=5600$  kPa, and  $T_0=295$  K. Since the sidewalls have no significant effect on the centerline flow field, only quasi-2D calculations were performed.

As shown in Fig. 4, the calculation accurately captures the shoulder expansion fan, the cowl-incident shock wave, and the reflected shock wave inside the throat. The flow field structure and the distribution of wall pressure at the upper and lower surfaces are generally consistent with the experimental results, which indicates that the numerical method is reliable.

To ensure the validity of the calculation method and boundary condition for supersonic boundary layer suction, the No. 101 suction plate of Eichorn et al. (2013) and Giehler et al. (2024) was used for numerical validation. The efficiency of the suction device is usually quantified by the sonic flow coefficient  $Q_{\text{sonic}}$  (Slater, 2012). It is defined as the ratio of the measured mass flow rate to the ideal mass flow rate under choked conditions:

$$Q_{sonic} = \frac{m}{\square}$$

$$m_{sonic}$$
(10)

$$m_{sonic} = Ap_0 \sqrt{\frac{\gamma}{RT_0}} \left(\frac{\gamma+1}{2}\right)^{-\frac{\gamma+1}{2(\gamma-1)}}$$
 (11)

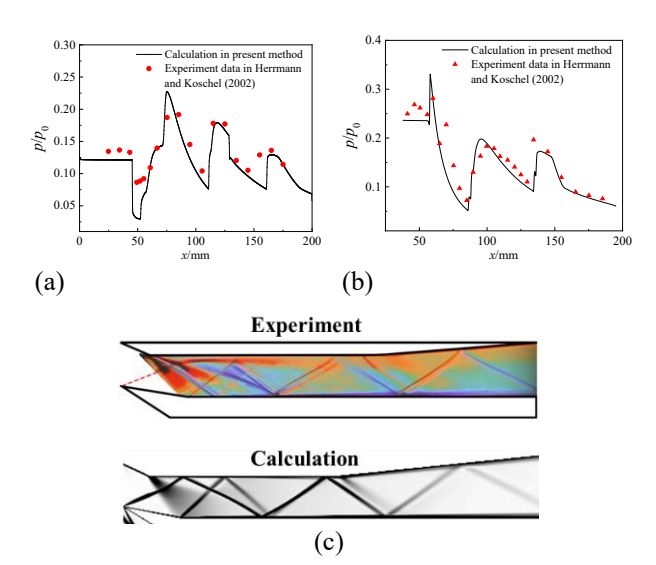


Fig. 4 Numerical validation of intake flow (experiment data in Herrmann and Koschel (2002)): the pressure distribution of (a)upper surface and (b) lower surface;(c) experimental and numerical schlieren

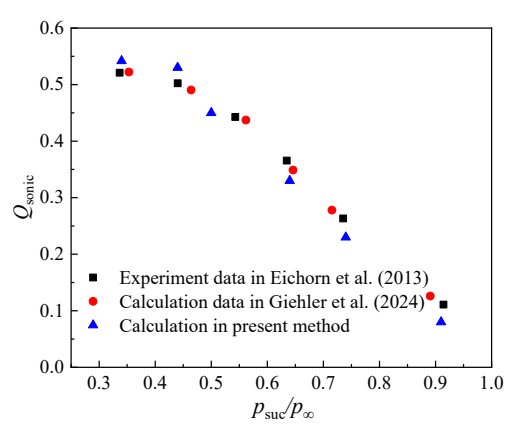


Fig. 5 Numerical validation of suction scheme with No. 101 plate: the sonic flow coefficient  $Q_{\text{sonic}}$ 

where A is the area of the suction hole, the hole diameter D is used in two-dimensional conditions. Since the flow direction in verification model (No. 101) is parallel to the wall, it is assumed that the pressure upstream of the inlet is the same as the local pressure at the suction hole. Therefore, the  $p_0$  and  $T_0$  were used to calculate the sonic flow coefficient  $Q_{\rm sonic}$ .

Only one hole of 6.35 mm diameter exists in the plate (No. 101) to obtain the mass flow rate. Figure 5 shows the variation of the sonic flow coefficient with suction backpressure. The numerical results are compared with the experimental and computational data of Eichorn et al. (2013) and Giehler et al. (2024). The calculation results remain consistent with the experimental results. Figure 6 shows the variation of the flow structure within the hole. As the backpressure increases, the flow in the suction hole is gradually blocked. The expansion angle at the leading edge of the hole gradually decreases, and the results are consistent with the previous study by Zhang et al. (2025). This indicates that the numerical method is able to meet the requirements of the suction scheme.

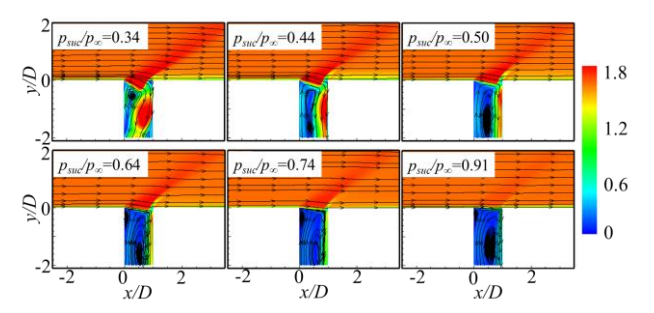


Fig. 6 Variation of flow field structure of No. 101 plate at different *P<sub>suc</sub>* 

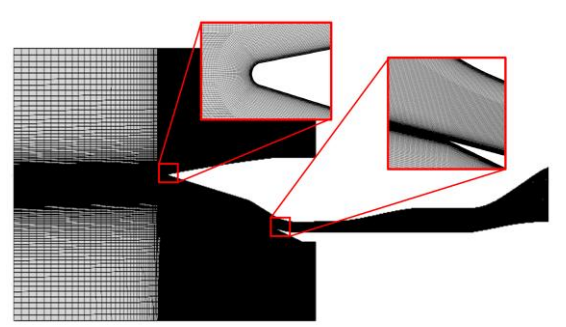


Fig. 7 Overall mesh distribution

Figure 7 illustrates the mesh distribution of the overall computational domain. Structural meshing was used to reduce the calculation time. The numerical model captures the geometric features of the rounded chamfers at the forebody's leading edge, and a suitable block structure is established using O-type meshing to ensure cell quality. For the near-wall and suction hole inner regions, the finer mesh resolution was used to identify the flow in the boundary layer accurately. Numerically, the turbulence modelling is satisfied by reducing the height of the first layer of the mesh to meet the  $y^{+} \le 1$ . The stretch factor of the mesh in the near-wall region is 1.1.

Since the discretization error and rounding error depend on the mesh resolution, coarse, fine, and dense mesh are designed for mesh-independence validation. As shown in Table 2, the total number of mesh elements is adjusted by varying the number of nodes, with three sets of meshes having 500,000, 1,000,000, and 2,000,000 elements, respectively. The heights of the first layer are 0.002 mm, 0.001 mm, and 0.0005 mm. The resulting  $y^+$ values are 1.9, 1.0, and 0.48, respectively. The mesh size in the flow direction is 0.35 mm, yielding maximum values of 175, 350, and 700 for the first layer mesh aspect ratios, respectively. Figure 8 illustrates the static pressure distribution on the compression face side for different mesh. The coarse mesh showed prediction errors at the pressure valley near the shock reflection. The pressure peak and rise plateau are accurately predicted using the fine mesh, whereas the dense mesh does not yield a

Table 2 Details of mesh resolution

| Level of   | Total number | Height of first | $v^{\scriptscriptstyle +}$ |  |
|------------|--------------|-----------------|----------------------------|--|
| resolution | of mesh      | layer (mm)      | y                          |  |
| Coarse     | 500,000      | 0.002           | 1.9                        |  |
| Fine       | 1,000,000    | 0.001           | 1.0                        |  |
| Dense      | 2,000,000    | 0.0005          | 0.48                       |  |

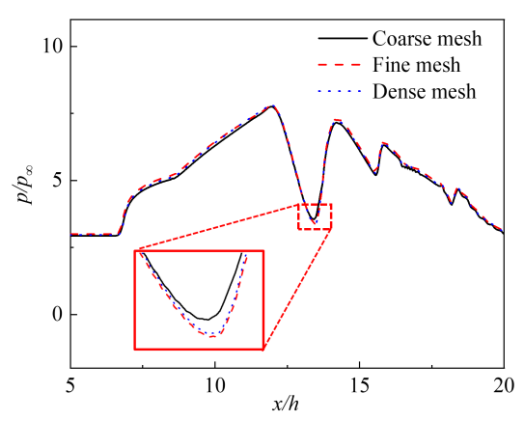


Fig. 8 Verification of mesh independence: the static pressure distribution on upper surface for different number of mesh

significant improvement. Therefore, mesh convergence is achieved. To maintain computational accuracy and economize time, a fine mesh is considered for all subsequent studies.

#### 3. RESULT AND DISCUSSION

# 3.1 Flow Characterization of the Base Model-Large Separation Pattern

The flow at the intake of a scramjet can be classified into three modes, i.e., subcritical, critical, and supercritical. Among them, the critical state is the design condition in which the shock waves converge at the cowl. Both subcritical and supercritical modes are off-design conditions. In the supercritical mode, the flow structure in the intake typically remains stable, with only some localized, low-amplitude oscillations of the SWBLI. However, in the subcritical mode, large-scale separation in the flow field and low-frequency oscillation are typically observed, where the oscillatory mode leads to significant fluctuations in TPR and CMFR, a phenomenon referred to as intake buzz. In this off-design condition, large-scale separation results in blockage, creating a narrower aerodynamic throat. The bow shock wave will be produced at the cowl, adding overflow to match the aerodynamic throat.

As shown in Fig. 9, the intake is under a typical subcritical state at Ma=3, and the shock waves generated by the two-stage compression surface of the forebody converge at the lower left side of the cowl. At the corner of the compression surface, the incoming boundary layer separates under the action of the compression shock and continues to the inlet. The large-scale separation occupies about 1/3 of the height at the inlet, and the aerodynamic throat height is only 2/3 of the original flow path. A blockage in the flow occurs, and the cowl forms a bowtype shock, overflowing fluid that cannot match the throat height of the outside. In this case, the pressure load at the cowl increases dramatically. As shown in Fig. 10, it is up to  $25.8p_{\infty}$ . After the incoming flow passes through the aerodynamic throat, a series of expansion waves are formed on the backwind side of the separation bubble, resulting in a localized decrease in pressure on the upper surface. In the circular section of the cowl, a series of

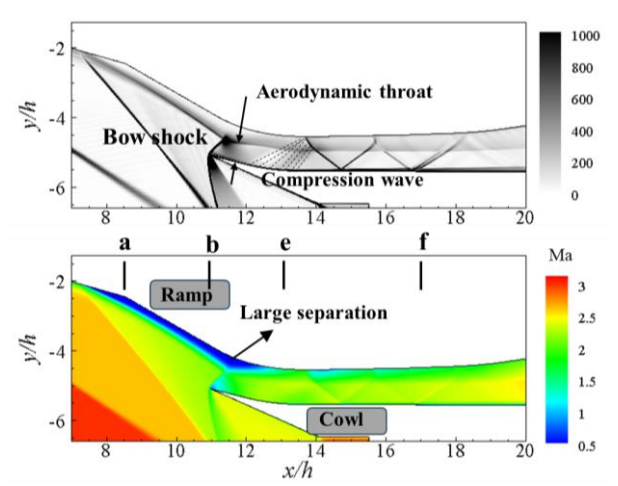


Fig. 9 Numerical schlieren and *Ma* contour for the Case 1

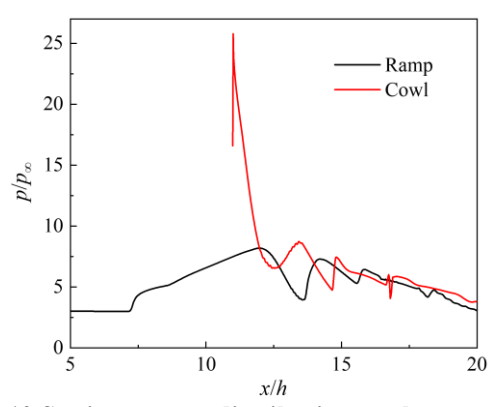


Fig. 10 Static pressure distribution on the ramp and cowl side of the Case 1

compression waves converge at the isolation, resulting in a localized increase in pressure values. The compression wave converges into an intense shock wave on the upper surface. It reflects downstream, forming multiple reflected shock waves in the isolated, manifesting as a wave-type on the wall pressure distribution curve. The incoming airflow flows to the diffusion section after multiple shock wave decelerations and pressurization. For the convenience of the following discussion, the regions at the inlet are named "a, b, e, and f," which correspond to the starting points of the compression corner, cowl, isolation, and diffusion, respectively.

#### 3.2 Suction Control in the Separation Zone

#### 3.2.1 Effect of Location/Number of Suction Holes

Figure 11 shows the numerical schlieren for different suction positions under the  $p_{\rm suc}/p_{\infty}=1$ . Gray-scale values indicate density variations in the flow field, and visualized flow features include compression shock, cowl incident shock, and obstacle shock generated at the trailing edge of the hole. The location of the turbulent boundary layer (TBL) is also clearly visible and marked with an orange dashed line. In the base model, the increased thickness of the boundary layer due to separation causes a blocked, bow-type shock wave to form at the cowl, resulting in deteriorated aerodynamic performance. After the incoming flow enters the inlet, the compression wave converges at the upper surface to create a shock wave and

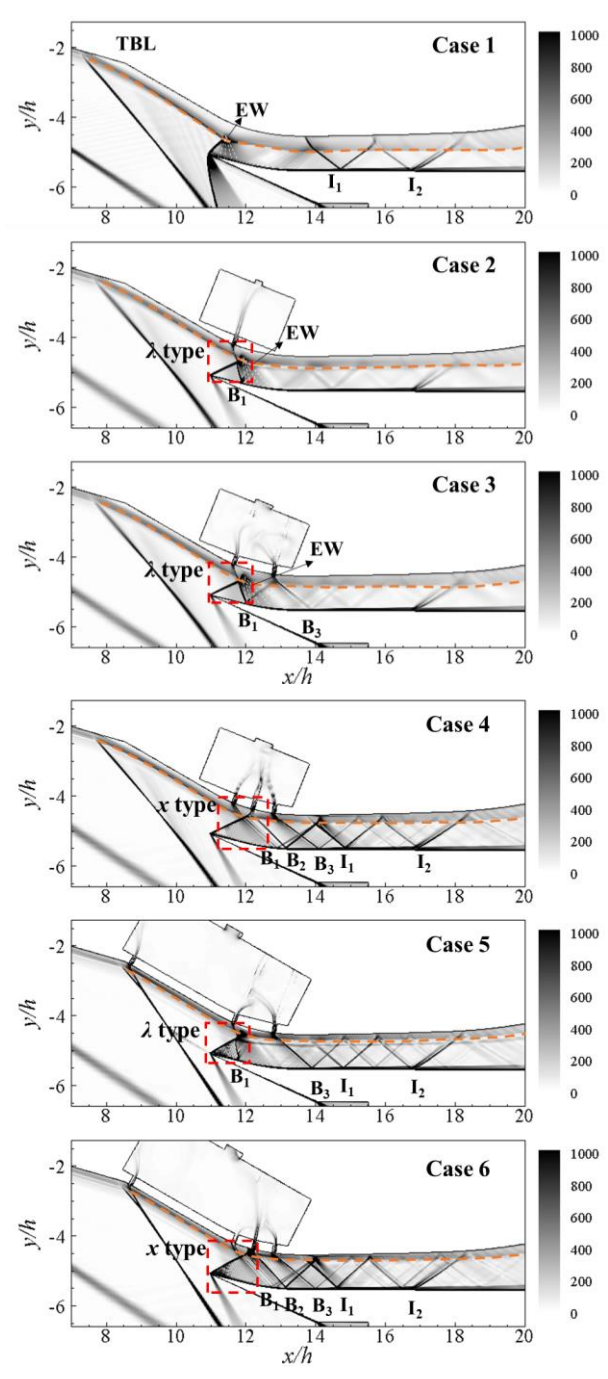


Fig. 11 Numerical schlieren for different number/position of suction holes at  $p_{suc}/p_{\infty}=1$ 

is incident at the lower surface  $I_1$ . With the opening of the holes  $S_1$ - $S_4$ , the thickness of the incoming boundary layer gradually decreases, the height of the aerodynamic throat increases, the incident shock wave is transformed into an oblique shock wave, and the adverse pressure gradient at the inlet is improved.

It should be noted that under the simplification of 2D flow, the suction effects of multiple holes cannot exhibit the staggered 3D phenomena observed in the study by Giehler et al. (2024). Instead, the flow characteristics resemble those of quasi-2D suction slots (Pattnaik and Rajan, 2022). In Case 2, only the  $S_1$  exists on the shoulder. The trailing edge of the suction hole inevitably generates a barrier shock and forms a " $\lambda$ " type shock interaction with

the cowl-incident shock. It leads to incident point B<sub>1</sub> on the lower surface at about x/h=11.9, and the intensity of the wave system is weakened. In Case 3, a portion of the low-energy flow in the channel is further removed under the action of  $S_1$  and  $S_3$ . It leads to an increase in the angle of the first reflected shock wave on the lower surface, and the B<sub>1</sub> is shifted downstream to approximately x/h=12.1. According to Green (1970), the structure of a typical SWBLI flow field reveals that an increase in the reflected shock angle will lead to a rapid enhancement of the total pressure loss, and consequently, a decrease in the TPR, which will be further discussed in Section 3.3. In Case 4,  $S_1$ ,  $S_2$ , and  $S_3$  exist simultaneously. Since  $S_2$  is located at the position of the incident point under suction control, the overflow reaches a significant level under a sizeable adverse pressure gradient, and the shock interaction at the inlet is transformed into an "x" type. Multiple shock reflections are formed within the isolator due to its regular wave system structure. In addition to the background wave system's action points I<sub>1</sub> and I<sub>2</sub>, the suction holes have three barrier shock wave action points (B<sub>1</sub>, B<sub>2</sub>, and B<sub>3</sub>). In Case 5, due to the closure of S2, an unbalanced adverse pressure gradient remains at the inlet, and the shock interaction is transformed into a "λ" type again. At this time, the wave system in the isolator is mainly formed by the barrier shock of  $S_3$  and the background wave system. Additionally, S<sub>4</sub> eliminates the separation bubble at the corner and reduces the boundary layer thickness. The foot of the secondary compression shock wave moves downstream, converging with the barrier shock, and is incident upstream of the cowl. In Case 6, the suction hole S<sub>2</sub> has been added, and the inlet has been transformed into an "x" type of shock interaction. The wave system is more prosperous, and the compression effect of the airflow will be more obvious.

For the two types of shock interaction at the inlet, Fig. 12(a) illustrates the difference in pressure contour. By extracting the pressure distribution at the position indicated by the red line in Fig. 12(a), Fig. 12(b) can demonstrate the variation of pressure values more clearly. In Case 3 and Case 5, the cowl shock interacts with the barrier shock of  $S_1$  in a " $\lambda$ " shape to produce a high-pressure region, resulting in a strong inverse pressure gradient at the inlet. The  $S_2$  significantly relieves the pressure environment and the " $\lambda$ " type shifts to the "x" type. As shown in Fig. 12(b), the change in the interaction type results in a significant decrease in the pressure peak at the centerline.

Figure 13 illustrates the distribution of the *Ma* contour. In the base model, a separation bubble is generated at the compression corner, pushing the shock wave upstream of the inflection point, creating an aerodynamic inflection point. The separation scale continues to the entrance and merges with the large-scale separation induced by the cowl shock. In Case 2, S<sub>1</sub> interrupted the continuity of the separation bubble. However, the separation at the compression surface and shoulder region remained. When both S<sub>1</sub> and S<sub>3</sub> are added, the scale of the shoulder separation decreases, and the position is locked in the middle of the two holes. In Case 4, the opening of S<sub>2</sub> drastically reduced the bubble size. The further opening of S<sub>4</sub> removes the bubble at the

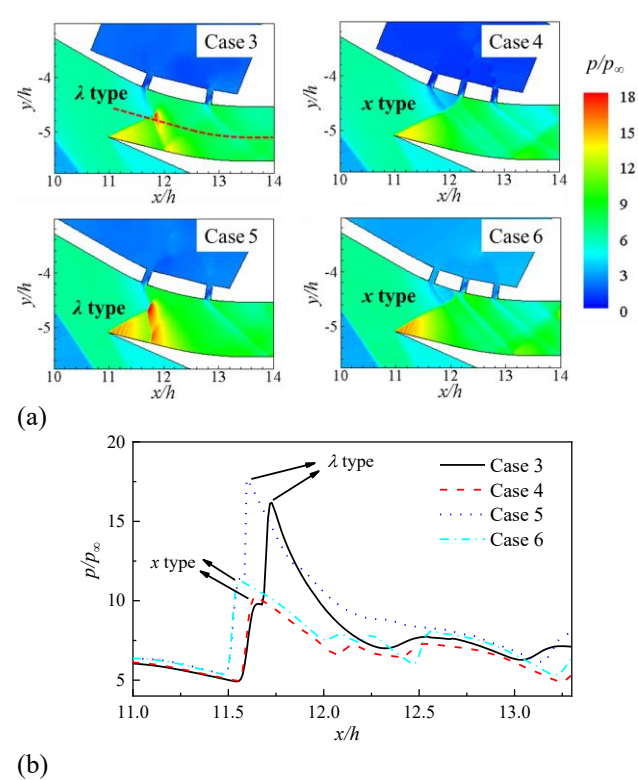


Fig. 12 Characteristic of pressure distribution for " $\lambda$ " and "x" type shock wave interaction: (a) the contour of pressure; (b) the extracted pressure profile

corner, reducing the incoming boundary layer thickness and realizing the maximum flow condition of the channel.

Figure 14 shows the Mach profile for different numbers/positions of suction holes. At point b, as shown in Fig. 14(a), the upper surface boundary layer of Case 1 produces a significant velocity deficit under a strong inverse pressure gradient. The thickness of boundary layer increases to x/h=4.4. Although the point b is located upstream of the hole, the inverse pressure gradient is improved by suction. The thickness of boundary layer decreases to x/h=4.18. It is worth noting that in Case 5 and Case 6, the application of S<sub>4</sub> at the corner results in a fuller boundary layer velocity profile. At point c, as shown in Fig. 14(b), the low kinetic energy fluid is substantially removed as the number of suction holes increases. The Mach profile gradually becomes full. Due to the application of a shoulder suction hole (S<sub>1</sub>), the separation bubble on the upper surface of the intake becomes locked downstream of the barrier shock (Zhang, et al., 2025), as observed in Cases 2, 3, and 5. The separation bubbles move closer to the entrance of the isolation section, which results in a larger deficit near the wall of the Mach number profile compared to Case 1. In Cases 4 and 6, the separation region is significantly reduced by S<sub>2</sub>, and the Mach number becomes larger.

The change in flow structure at the suction holes for Case 2-4 is given in Fig. 12. As the number of shoulder suction holes increases, the scale of the separation zone decreases. Typical supersonic under-expanded jets are formed in the suction holes due to the acceleration of the low-pressure environment at the outlet. In Case 2, the separating bubble is locked downstream of the barrier shock in  $S_1$ . In Case 3, which is located between the two

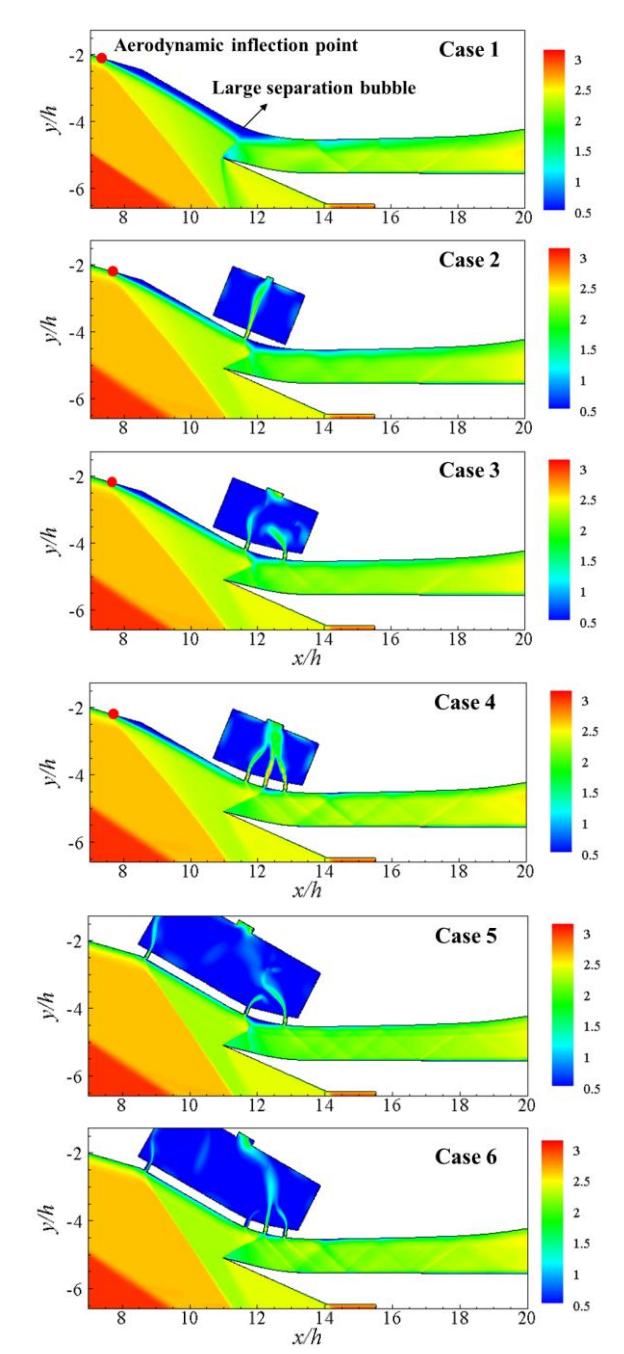


Fig. 13 Contour of Ma for different number/position of suction holes at  $p_{\rm suc}/p_{\infty}=1$ 

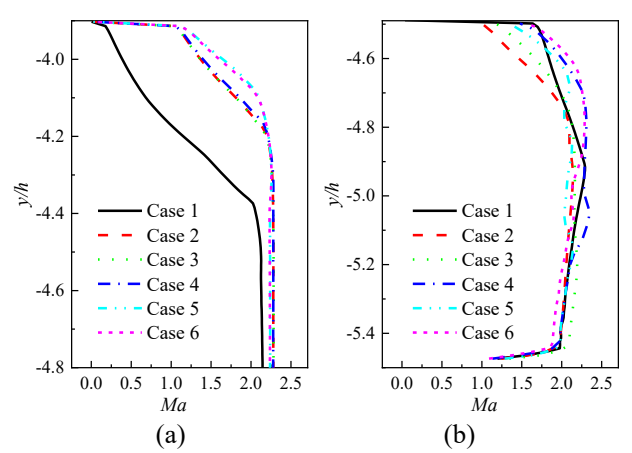
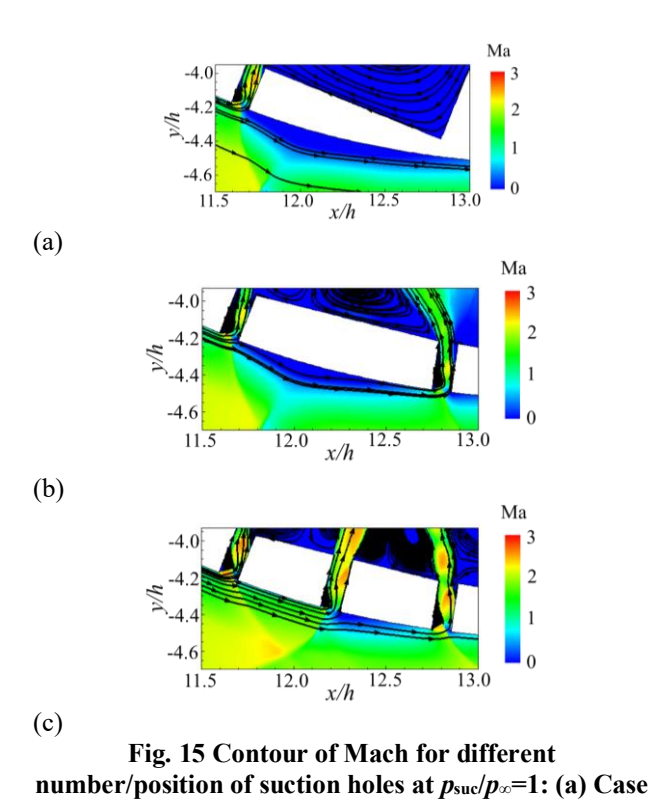


Fig. 14 Mach profile for different number/position of suction holes at  $p_{\text{suc}}/p_{\infty}=1$ : (a) at point b; (b) at point c

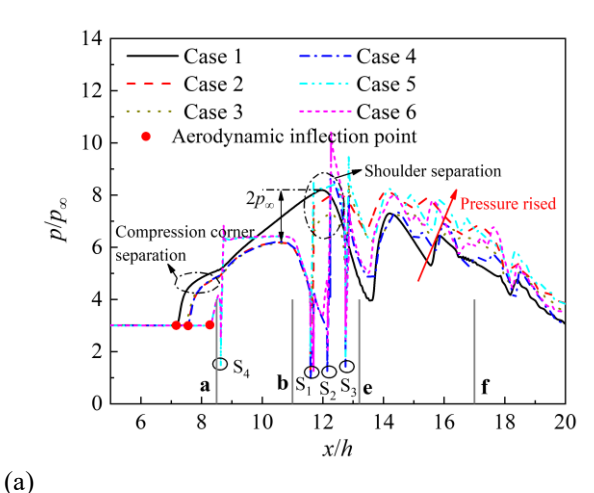


2; (b) Case 3; (c) Case 4
holes. In Case 4, a deflection of the flow at the suction hole

holes. In Case 4, a deflection of the flow at the suction hole is observed, implying that part of the local boundary layer is removed.

To further discuss the effect of suction holes on the intake loading environment, Fig. 16 shows the pressure distribution along the wall. The step feature at the S<sub>1</sub>-S<sub>4</sub> position is demonstrated in all pressure distribution curves, where the pressure first decreases due to the expansion wave at the leading edge, followed by a sudden rise due to the barrier shock wave at the trailing edge. In Fig. 16(a), Case 1 shows the first pressure rise in response to a compression shock at the aerodynamic inflection point. The position is at x/h=7.2, 1.3h more upstream than the geometric inflection point. In Case 2-Case 4, the aerodynamic inflection point moved downstream by 0.3h under the suction action of S<sub>1</sub>-S<sub>3</sub>, even though S<sub>4</sub> was permanently closed. Furthermore, with the opening of S<sub>4</sub>, the local suction removes most of the low-energy flow, and the shock approaches position "a." The maximum drop in wall pressure at "b" is up to  $2p_{\infty}$  because the suction relieves the entrance blockage. In the S2-closed state (e.g., Case 2, 3, 5), a separation pressure plateau can all be observed in the "b-e" section, consistent with the flow field results in Fig. 13.

The pressure distribution along the lower surface is shown in Fig. 16(b). Under the action of the bow shock, the incoming flow is almost close to stagnation at the cowl, and the wall pressure reaches 25.8  $p_{\infty}$ . The suction effect converts the cowl incident shock wave to an oblique shock. The inlet blockage has been improved; thus, the wall static pressure has decreased substantially. The drop is up to 12.2  $p_{\infty}$ , 47.3% of the base model. It is worth noting that in Case 2, Case 3, and Case 5, the separation bubbles at the shoulder not be removed entirely due to the closure of  $S_2$ , and the " $\lambda$ " type of shock interaction is



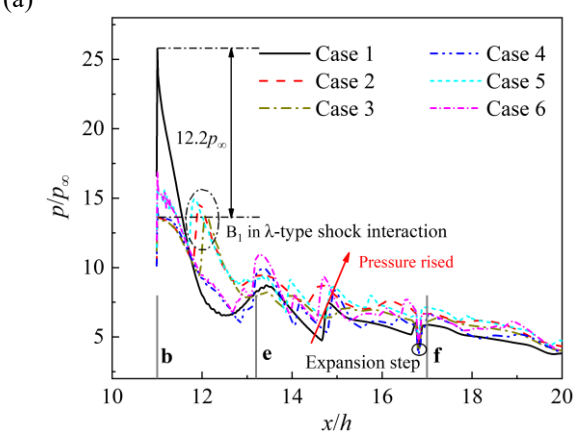


Fig. 16 Static pressure distribution for different number/position of suction holes at at  $p_{\text{suc}}/p_{\infty}=1$ : (a) upper surface (b) lower surface

formed at the entrance (shown in Fig. 11). The shock incident point  $B_1$  on the lower surface is closer to the cowl "b." It exhibits a higher amplitude on pressure distribution. Therefore, the suction hole ( $S_2$ ) at the location of the shock incident point dominates the boundary layer suction in the inlet, consistent with the results of Zhang et al. (2025). In the region of section "e-f," the wave system of the isolator in the controlled state is more abundant, and the airflow pressurization is more prominent. Correspondingly, the wall static pressure in Cases 2-5 is higher than in Case 1.

# 3.2.2 Effect of Backpressure of Suction Holes

Different backpressures through the chamber generate different flow rates in the suction holes. Figure 17 shows the numerical schlieren and Ma contour for different suction backpressures in Case 4. With the gradual increase of backpressure, the flow inside  $S_1$  is first weakened. Due to the pressure gradient formed by the incident shock, the flow within  $S_2$  is always stronger than  $S_1$  and  $S_3$ , which demonstrates the advantage of flow removal in  $S_2$ .

Figure 18 shows the numerical schlieren and Ma contour in Case 6. Due to the increase of  $S_4$ , the separation bubble at the inflection point (shown in Fig. 18(b)) is completely removed with sufficient suction intensity. The Mach number increases, and the kinetic energy of the airflow is enhanced. As the suction backpressure increases, when  $p_{suc}/p_{\infty}=5$ , the suction strength of  $S_4$  is not

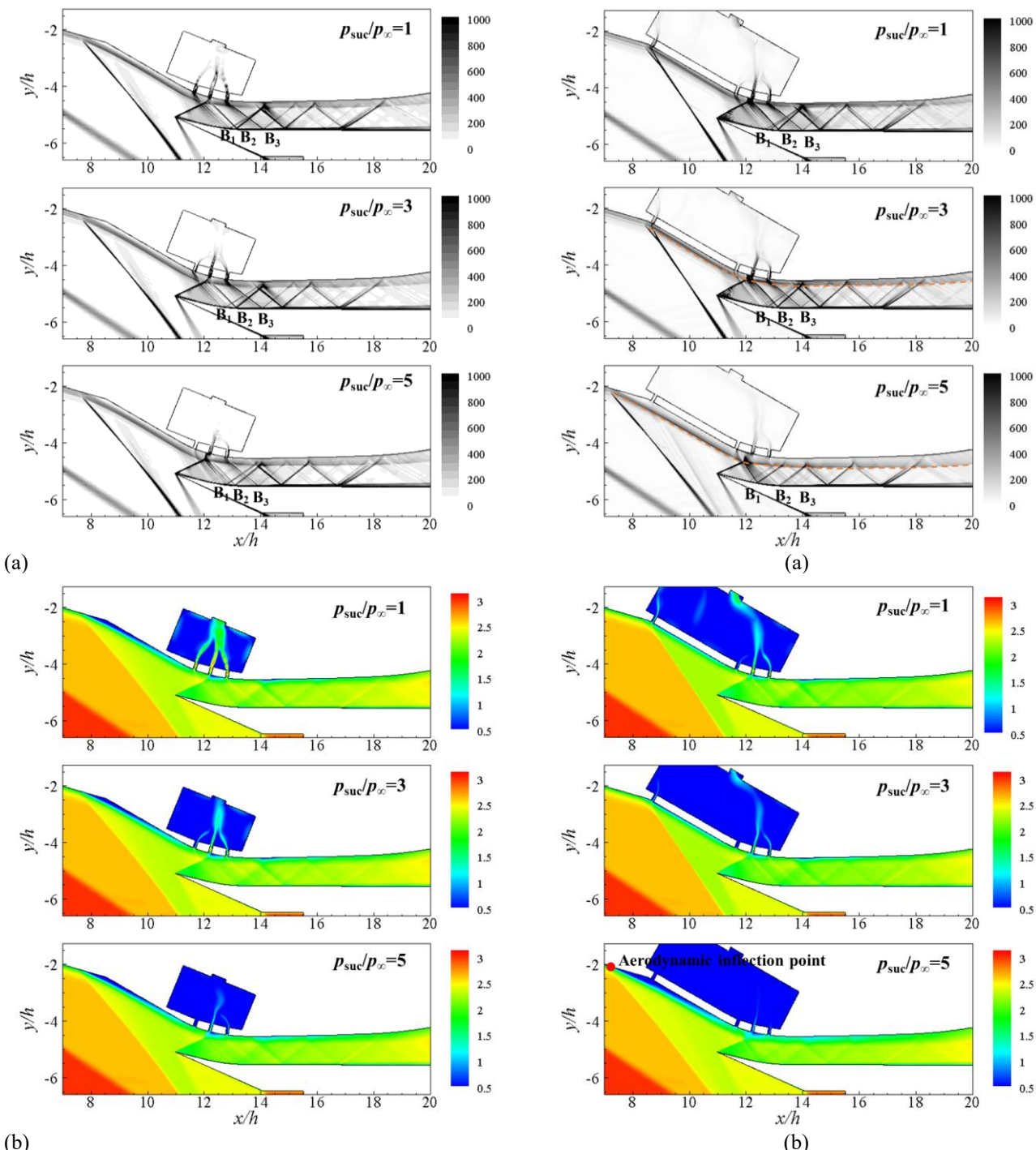


Fig. 17 Numerical schlieren and *Ma* contour for different suction backpressure in Case 4: (a)
Numerical schlieren (b) *Ma* contour

Fig. 18 Numerical schlieren and *Ma* contour for different suction backpressure in Case 6: (a) Numerical schlieren (b) *Ma* contour

enough to remove the separation bubble at the inflection point. The aerodynamic inflection point reappears and returns to the upstream region. Additionally, the thickness of the boundary layer downstream of the suction hole increases gradually with the increase in suction backpressure. After the thickness of the boundary layer is increased, the shock interaction at the entrance changes back to the " $\lambda$ " type. At the same time, the positions of the barrier shock wave incident points  $B_1$ ,  $B_2$ , and  $B_3$  are changed accordingly.

The change in position of B<sub>1</sub> with the change in back pressure is given in Fig. 19, while the bleed mass flow

(*BMF*) of the suction holes is plotted. The *BMF* is defined as:

$$BMF = \stackrel{\bullet}{m}_{iso} - \stackrel{\bullet}{m}_{in} \tag{12}$$

where  $\dot{m}_{iso}$  is the mass flow captured at the entrance "e" of the isolator and  $\dot{m}_{in}$  is the actual mass flow captured at entrance "b".

With the increase in backpressure, the *BMF* gradually decreases. The suction hole forms the blockage, and the low-kinetic fluid in the boundary layer is not removed. Accordingly, the  $B_1$  gradually shifts from x/h=12.72 to

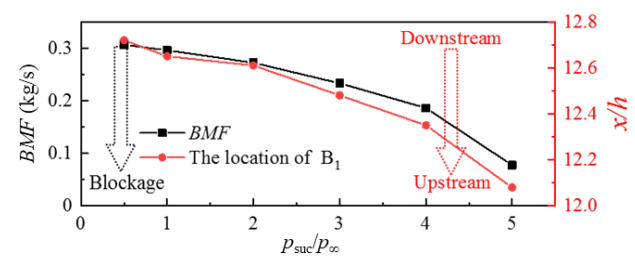


Fig. 19 Variation of *BMF* and B<sub>1</sub> points with backpressure in Case 6

x/h=12.07, leading to a change in the shock interaction to the " $\lambda$ " type, and the intensity of the wave system is weakened.

#### 3.3 Performance of Controlled Intake

To further evaluate the variation in intake performance under boundary layer suction, equations (13)-(18) were used to characterize the aerodynamic properties.

(i) Total Pressure Recovery (*TPR*): The *TPR* reflects the degree to which the total pressure of the airflow is maintained within the intake. It also measures the total pressure loss during compression from another perspective. The greater the *TPR*, the smaller the total pressure loss and the higher the energy utilization efficiency. It is defined as the ratio of the total pressure at the outlet "f" of the isolation to the incoming total pressure.

$$TPR = \frac{\overline{p_{0-iso}}}{p_0} \times 100\%$$
 (13)

where  $\frac{p_0}{p_{0-iso}}$  is the total pressure at the outlet of isolator and  $p_0$  is the incoming total pressure.

(ii) Captured Mass Flow Ratio (*CMFR*): The *CMFR* reflects the intake's efficiency in capturing airflow under different conditions. It is defined as the ratio of the actual captured mass flow rate at the inlet to the theoretical captured mass flow rate.

$$CMFR = \frac{m_{in}}{\bullet} \times 100\%$$

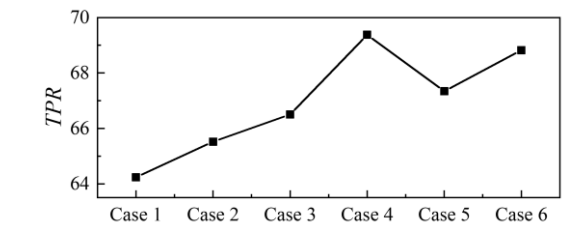
$$m_{theory}$$
(14)

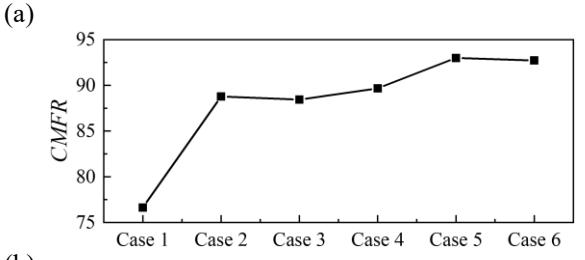
where  $m_{theory}$  is the theoretical capture mass flow rate. It can be solved by the  $\theta$ - $\beta$ -Ma equation for oblique shock in the inviscid relation.

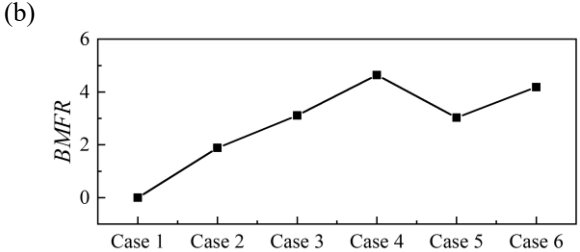
$$\tan \theta = \frac{\cot \beta \, (Ma_1^2 \sin^2 \beta - 1)}{Ma_1^2 \left( (\gamma + 1) / 2 - \sin^2 \beta \right) + 1}$$
 (15)

$$Ma_2^2 = \frac{2 + (\gamma - 1)(M_1 \sin \beta)^2}{\left[2\gamma(M_1 \sin \beta)^2 - (\gamma - 1)\right]\sin^2(\beta - \theta)}$$
 (16)

where  $\theta$  is the flow deflection angle,  $\beta$  is the oblique shock angle,  $Ma_1$  is the Mach number of the wave front, and  $Ma_2$  is the Mach number of the wave behind. The Ma behind the secondary compression wave is obtained through an iterative solution, and the theoretical mass flow rate is calculated to be 10.8 kg/s.







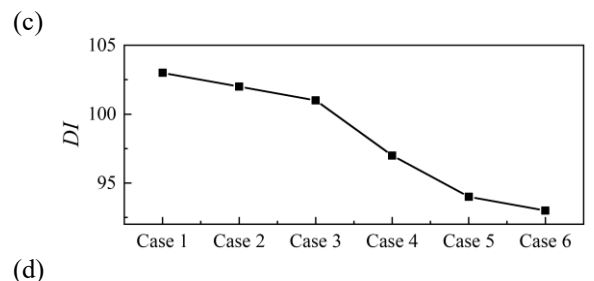


Fig. 20 Variation of the aerodynamic performance with suction: (a) TPR; (b) CMFR; (c) BMFR; (d) DI

(iii) Bleed Mass Flow Ratio (*BMFR*): The *BMFR* reflects the ability to remove low-kinetic-energy airflow during boundary-layer suction. It is defined as the ratio of the boundary-layer bleed mass flow rate to the captured mass flow rate at the inlet.

$$BMFR = \frac{m_{in} - m_{iso}}{\bullet} \times 100\%$$

$$(17)$$

(iv) Distortion Index (DI): the DI measures the flow distortion at the outlet of the isolator and is defined by the uniformity of the total pressure distribution.

$$DI = \frac{p_{0-iso-max} - p_{0-iso-min}}{p_{0-iso}} \times 100\%$$
 (18)

where  $p_{0-iso-max}$  is the maximum total pressure at the outlet of the isolator and  $p_{0-iso-min}$  is the minimum.

Figure 20 exhibits the variation of intake aerodynamic performance indexes for different configurations. The *TPR* and *CMFR* are low in the off-designed state, while the *DI* reaches 103% (Case 1). Under the deterioration of aerodynamic performance, the insufficient captured airflow and significant flow distortion easily lead to engine shutdown or oscillation, which is not conducive to safe and stable operation. Significant performance

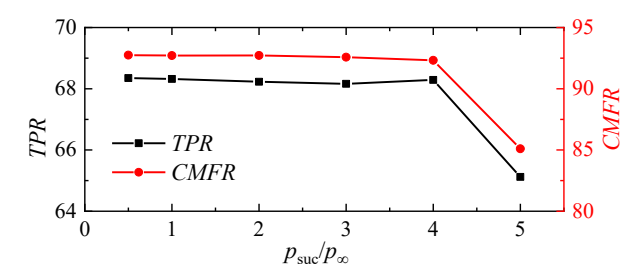


Fig. 21 Variation of *TPR* and *CMFR* with different suction backpressure in Case 6

improvements occurred when the suction device was added. In particular, the TPR increased to a maximum of 69.4% (Case 4), representing a 5.2% improvement over Case 1, thereby enhancing compression efficiency. The CMFR increased to a maximum of 93.0% (Case 5), a 16.4% increase compared to Case 1, dramatically improving flow capture. However, the BMFR at this point was only 3.0%, and the effect of boundary layer suction the mainstream remained relatively Additionally, the removal of low-energy fluid within the boundary layer reduced flow distortion. The DI was minimally reduced to 93.0% (Case 6), 10.0% lower than in Case 1. In both Case 4 and Case 6, the TPR increased by approximately 5%, and the CMFR increased by more than 13%, demonstrating the importance of S<sub>2</sub> at the shoulder for aerodynamic performance. From the change in DI, the main advantage of S<sub>4</sub> is the reduction of separation upstream of the entrance, which reduces the degree of flow distortion.

Figure 21 shows the *TPR* and *CMFR* trend in Case 6 under varying backpressure. When  $p_{\text{suc}}/p_{\infty} < 4.0$ , both *TPR* and *CMFR* remained broadly stable. It is due to the fact that in Case 6, the suction holes were opened, and the flow in the holes reached saturation under low backpressure. Although the flow within the holes is still sufficient to remove the same degree of boundary layer components as the backpressure increases over a small range. As the backpressure increases to  $p_{\text{suc}}/p_{\infty}=5$ , the flow in the holes is gradually restricted. The suction becomes weaker, the boundary layer thickens, and the type of shock interaction at the entrance changes, as shown in Fig. 18, at which point both the *TPR* and *CMFR* of the intake decrease precipitously.

# 4. CONCLUSION

Boundary layer suction provides an effective means of controlling flow in the intake under off-design conditions, substantially improving aerodynamic performance. Numerical simulations are performed to investigate the mechanism of suction under off-design conditions and its effect on aerodynamic performance. The main conclusions are as follows:

(1) The location/number of boundary layer suction holes has a significant effect on the flow structure. The suction device effectively removes low-kinetic-energy fluid, relieving the inlet blockage condition. It leads to the transformation of bow shock to oblique shock at the cowl, and the height of the aerodynamic throat increases significantly. The  $S_2$  at the incident point of the cowl shock

has a key role in controlling the separation bubble. The  $S_4$  at the compression corner regulates the flow structure by changing the position of the aerodynamic inflection point. The increase in the number of suction holes leads to a gradual shift of the shock interaction from the " $\lambda$ " to the " $\lambda$ " type. The wave reflection phenomenon is evident, and the airflow compression is enhanced.

- (2) Boundary layer suction can effectively improve the aerodynamic performance of the intake. Compared to the base model, the reasonable setting of suction holes can increase the *TPR* by a maximum of 5.2% and the *CMFR* by a maximum of 16.4%, while the *DI* is significantly reduced by 10.0%.
- (3) The backpressure of the suction also has an important effect on the flow structure. As the backpressure increases, the *BMFR* decreases. The low-kinetic fluid within the boundary layer cannot be removed, resulting in an increase in thickness at the boundary and an upward shift in the location of the shock incident point. As the  $p_{\text{suc}}/p_{\infty}$  increases to 5, the shock interaction at the entrance changes, and the *TPR* and *CMFR* decrease precipitously.

In summary, boundary layer suction is an effective technique for controlling the shock structure and improving the aerodynamic performance of the intake under off-design conditions. Although efficiency is largely constrained by the location/number and backpressure of suction holes, the technique still has important engineering applications for improving the performance of supersonic intakes.

# ACKNOWLEDGEMENTS

This work was supported by the National Nature Science Foundation of China (Grant No. 52130603, and 12402409) and Sichuan Provincial Natural Science Foundation (Grant No. 2024NSFSC0958), which is gratefully acknowledged.

#### **CONFLICT OF INTEREST**

The authors have no conflicts to disclose.

#### **AUTHORS CONTRIBUTION**

Yaowen Zhang: Formal analysis (equal); Methodology (equal); Writing-original draft (equal); Writing-review & editing (equal); Dangguo Yang: Writing-review & editing (equal); Supervision (equal). Bin Dong: Writing-review & editing (equal). Supervision (equal); Shaozhan Wang: Data curation (equal); Formal analysis (equal).

# REFERENCES

Abedi, M., Askari, R., & Soltani, R. (2020a). Numerical simulation of inlet buzz. *Aerospace Science and Technology*, 97, 105547. https://doi.org/10.1016/j.ast.2019.105547

Abedi, M., Askari, R., Sepahi J., & Soltani, R. (2020b). Axisymmetric and three-dimensional flow simulation

- of a mixed compression supersonic air inlet. *Propulsion and Power Research*, 9(1), 51-61. <a href="https://doi.org/10.1016/j.jppr.2020.01.002">https://doi.org/10.1016/j.jppr.2020.01.002</a>
- Alfonsi, G. (2009). Reynolds-Averaged Navier-Stocks Equations for Turbulence Modeling. *Applied. Mechanics Reviews*, 62, 933–944. <a href="https://doi.org/10.1115/1.3124648">https://doi.org/10.1115/1.3124648</a>
- Chen, H., Tan, H., Liu, Y., & Zhang, Q. (2019). External-compression supersonic inlet free from violent buzz. AIAA Journal, 57(6), 2513–2523. https://doi.org/10.2514/1.J057811
- Choe, Y., Kim, C., & Kim, K. (2020). Effects of optimized bleed system on supersonic inlet performance and buzz. *Journal of Propulsion and Power*, *36*(2), 211-222. https://doi.org/10.2514/1.B37474
- Eichorn, M., Barnhart, P., Davis, D., Vyas, M., & Slater, J. (2013). Effect of boundary-layer bleed hole inclination angle and scaling on flow coefficient behavior. In 51st AIAA Aerospace Sciences Meeting including the New Horizons Forum and Aerospace Exposition, 424. https://doi.org/10.2514/6.2013-424
- Fisher, A. (1986). Three-dimensional flow effects in a two-dimensional supersonic air intake. *Journal of Propulsion and Power*, 2(6), 546-551. <a href="https://doi.org/10.2514/3.22940">https://doi.org/10.2514/3.22940</a>
- Fukuda, M., Hingst, W., & Reshotko, E. (1977). Bleed effects on shock/boundary-layer interactions in supersonic mixed compression inlets. *Journal of Aircraft*, 14(2), 151–156. https://doi.org/10.2514/3.58756
- Giehler, J., Grenson, P., & Bur, R. (2024). Parameter influence on porous bleed performance for supersonic turbulent flows. *Journal of Propulsion and Power*, 40(1), 74-93. https://doi.org/10.2514/1.B39236
- Green, J. (1970). Interaction between shock waves and turbulent boundary layers. *Progress in Aerospace Sciences*, 11, 235-340. <a href="https://doi.org/10.1016/0376-0421(70)90018-7">https://doi.org/10.1016/0376-0421(70)90018-7</a>
- Hamed, A., Yeuan, J., & Shih, S. (1995). Shock-wave/boundary-layer interactions with bleed. II effect of slot location. *Journal of Propulsion and Power*, 11(6), 1236–1241. https://doi.org/10.2514/3.23963
- He, Y., Huang, H., & Yu, D. (2017). Investigation of corner separation and suction control in constant area duct. *Aerospace and Science Technology*, 66, 70-82. <a href="https://doi.org/10.1016/j.ast.2017.01.029">https://doi.org/10.1016/j.ast.2017.01.029</a>
- Herrmann, C., & Koschel, W. (2002). Experimental investigation of the internal compression inside a hypersonic intake, In 38th AIAA/ASME/SAE/ASEE Joint Propulsion Conference & Exhibit, 4130. https://doi.org/10.2514/6.2002-4130
- Herrmann, D., Blem, S., & Gulhan, A. (2011). Experimental study of boundary-layer bleed impact on ramjet inlet performance. *Journal of Propulsion and Power*, 27 (6), 1186–1195 <a href="https://doi.org/10.2514/1.B34223">https://doi.org/10.2514/1.B34223</a>

- Herrmann, D., Siebe, F., & Gulhan, A. (2013). Pressure Fluctuations (Buzzing) and Inlet Performance of an Airbreathing Missile. *Journal of Propulsion and Power*, 29(4), 839–848. https://doi.org/10.2514/1.B34629
- Hirschen, C., Herrmann, D., & Gülhan, A. (2007). Experimental investigations of the performance and unsteady behaviour of a supersonic intake. *Journal of Propulsion and Power*, 23(3), 566–574. <a href="https://doi.org/10.2514/1.25103">https://doi.org/10.2514/1.25103</a>
- Khan, A., Chidambaranathan, M., Verma, S., & Kumar, R. (2023) Swept shock/boundary-layer interaction control using micro-vortex generators. *Shock Waves*, 33(7), 553-567. <a href="https://doi.org/10.1007/s00193-023-01155-0">https://doi.org/10.1007/s00193-023-01155-0</a>
- Kwak, E., & Lee, S. (2013). Numerical study of the effect of exit configurations on supersonic inlet buzz. In 31st AIAA Applied Aerodynamics Conference, San Diego, California. <a href="https://doi.org/10.2514/6.20133025">https://doi.org/10.2514/6.20133025</a>
- Liou, M., & Benson, T. (2010). *Optimization of Bleed for Supersonic Inlet*. In 13th AIAA/ISSMO multidisciplinary analysis optimization conference, 2010-9172. <a href="https://doi.org/10.2514/6.2010-9172">https://doi.org/10.2514/6.2010-9172</a>
- Menter, F. (1994). Two-equation eddy-viscosity turbulence models for engineering applications. *AIAA Journal*, 32(8), 1598-1605. https://doi.org/10.2514/3.12149
- Narayanaswamy, M., & Funderburk, V. (2019). Experimental investigation of microramp control of an axisymmetric shock/boundary layer interaction. *AIAA Journal*, 57(4), 1594–1607. https://doi.org/10.2514/1.J057846
- Pattnaik, S., & Rajan, N. (2022). Numerical investigation of impact of fixed-exit boundary-layer bleed on supersonic intake performance. *Aerospace Science and Technology*, 120, 107286. https://doi.org/10.1016/j.ast.2021.107286
- Schülein, E., Schnepf, C., & Weiss, S. (2022). Concave bump for impinging-shock control in supersonic flows. *AIAA Journal*, 60(5), 2749–2766. https://doi.org/10.2514/1.J060799
- Sethuraman, V., Kim, T., & Kim, H. (2021). Control of the oscillations of shock train using boundary layer suction. *Aerospace and Science Technology*, 118, 107012. https://doi.org/10.1016/j.ast.2021.107012
- Slater, J. W. (2012). Improvements in modeling 90-degree bleed holes for supersonic inlets. *Journal of Propulsion and Power*, 28(4), 773-781. https://doi.org/10.2514/1.B34333
- Soltani, M., Daliri, A., Younsi, J., & Farahani, M. (2016). Effects of bleed position on the stability of a supersonic inlet. *Journal of Propulsion and Power*, 32(5), 1153-1166. https://doi.org/10.2514/1.B36162
- Soltani, M., Younsi, J., & Farahani, M. (2015). Effects of boundary-layer bleed parameters on supersonic intake performance. *Journal of Propulsion and Power*, 31(3), 826–836. https://doi.org/10.2514/1.B35461

- Tian, S., Jin, L., Huang, W., & Shen, Y. (2023). Surrogate-based optimization on bump for shock wave/boundary layer interaction control. *Acta Astronautica*, 212, 139-151. <a href="https://doi.org/10.1016/j.actaastro.2023.08.008">https://doi.org/10.1016/j.actaastro.2023.08.008</a>
- Titchener, N., & Babinsky, H. (2013). Shock wave/boundary-layer interaction control using a combination of vortex generators and bleed. *AIAA Journal*, 51(5), 1221–1233. <a href="https://doi.org/10.2514/1.J052079">https://doi.org/10.2514/1.J052079</a>
- Wang, B., Sandham, N., Hu, Z., & Liu, W. (2015). Numerical study of oblique shock-wave/boundary-layer interaction considering sidewall effects. *Journal of Fluid Mechanics*, 767, 526-561. https://doi.org/10.1017/jfm.2015.58
- Wang, Z., Chang, J., Li, Y., & Kong, C. (2021). Investigation of shock wave control by suction in a supersonic cascade. *Aerospace Science and Technology*, 108, 106382. <a href="https://doi.org/10.1016/j.ast.2020.106382">https://doi.org/10.1016/j.ast.2020.106382</a>
- Wilcox, D. (1998). *Turbulence Modeling for CFD*. DCW Industries: La Canada, CA, USA.
- Wong, W. (1974). The application of boundary layer suction to suppress strong shock-induced separation in supersonic inlets. In *10th Propulsion Conference*, 1974-1063. https://doi.org/10.2514/6.1974-1063
- Yamamoto, J., Kojima, Y., Kameda, M., Watanabe, Y., Hashimoto, A., & Aoyama, T. (2020). Prediction of the onset of supersonic inlet buzz. *Aerospace Science and Technology*, 96, 105523.

# https://doi.org/10.1016/j.ast.2019.105523

- Zhang, J., Yuan, H., Wang, Y., & Huang, G. (2020). Experiment and numerical investigation of flow control on a supersonic inlet diffuser. *Aerospace and Science Technology*, 106, 106182. https://doi.org/10.1016/j.ast.2020.106182
- Zhang, Y., Tan, H., Du, M., & Wang, D. (2015). Control of shock/ boundary-layer interaction for hypersonic inlets by highly swept microramps. *Journal of Propulsion and Power*, 31(1), 133-143. https://doi.org/10.2514/1.B35299
- Zhang, Y., Tan, H., Li, J., & Yin, N. (2019). Control of cowl-shock/boundary-layer interactions by deformable shape-memory alloy bump. *AIAA Journal*, *57*(2), 696–705. <a href="https://doi.org/10.2514/1.J057409">https://doi.org/10.2514/1.J057409</a>
- Zhang, Y., Wang, S., Yang, D., & Dong, B. (2025). Numerical Study on the Influence of Suction near Expansion Corner on Separation Bubble. *Aerospace*, 12(2), 89. https://doi.org/10.3390/aerospace12020089
- Zhou, Y., Zhao, Y., & Zhao, Y. (2019). A study on the separation length of shock wave/turbulent boundary layer interaction. *International Journal of Aerospace Engineering*, 2019(1), 8323787. https://doi.org/10.1155/2019/8323787
- Zuo, F., & Huang, G. (2018). Numerical investigation of bleeding control method onsection-controllable wave-catcher intakes. *Acta Astronaut*, *151*, 572–584. <a href="https://doi.org/10.1016/j.actaastro.2018.06.059">https://doi.org/10.1016/j.actaastro.2018.06.059</a>